

Supplementary Materials for

Intelligent optoelectrowetting digital microfluidic system for real-time selective parallel manipulation of biological droplet arrays

Tianyi Wang,^{a, b†} Shizheng Zhou,^{c†} Xuekai Liu,^a Jianghao Zeng,^a Xiaohan He,^{a, b} Zhihang Yu,^d

Zhiyuan Liu,^e Xiaomei Liu,^a Jing Jin,^d Yonggang Zhu,^d Liuyong Shi,^{*a} Hong Yan,^{*f} and Teng Zhou^{*a}

^a School of Mechanical and Electrical Engineering, Hainan University, Haikou 570228, Hainan, China

^b School of Information and Communication Engineering, Hainan University, Haikou 570228, Hainan, China

^c Institute of Applied Physics and Materials Engineering, University of Macau, Macau 999078, China

^d Center for Microflows and Nanoflows, School of Mechanical Engineering and Automation, Harbin Institute of Technology, Shenzhen, Shenzhen 518055, China

^e School of Marine Biology and Fisheries, Hainan University, Haikou 570228, China

^f School of Computer Science and Technology, Hainan University, Haikou 570228, Hainan, China

†These authors contributed equally

Correspondence: Liuyong Shi; Teng Zhou. School of Mechanical and Electrical Engineering, Hainan University, Haikou 570228, Hainan, China; Email: shiliuyong@hainanu.edu.cn; zhouteng@hainanu.edu.cn. Hong Yan. School of Computer Science and Technology, Hainan University, Haikou 570228, Hainan, China. Email: yanhong@hainanu.edu.cn.

This PDF file includes:

Supplementary S1. Optoelectrowetting digital microfluidic platform

Supplementary S2. OICS software interface

Supplementary S3. Overview of OICS operation process

Supplementary S4. Impact of luminance on detection

Supplementary S5. Chip fabrication process

Supplementary S6. OEW chip

Supplementary S7. Photolithography process for droplet storage reservoir

Supplementary S8. Model comparison and training

Supplementary S9. Tracking and matching process of the ByteTrack algorithm

Supplementary S10. Comparison of droplet speed at different frequencies

Supplementary S11. Droplet behavior at different voltages

Supplementary S12. Culturing with 0X0 and 1X1 medium containing dye in 96-well plates

Supplementary S13. Characterization of chlorella cultured in 96-well plates on hemocytometer

Supplementary S14. Comparison of projected optical patterns

Supplementary Table S1. Customized BG11 medium composition table

Other Supplementary Materials for this manuscript include the following:

Supplementary Movies S1 (.mp4 format). Droplet movement from 100Hz to 500Hz at 70V (microscope, 1X)

Supplementary Movies S2 (.mp4 format). Droplet movement with deviation discrimination (microscope, 1X)

Supplementary Movies S3 (.mp4 format). Droplet movement with deviation discrimination (software, 3X)

Supplementary Movies S4 (.mp4 format). Intelligent parallel manipulation of droplet arrays (microscope, 1X)

Supplementary Movies S5 (.mp4 format). Intelligent parallel manipulation of droplet arrays (software, 3X)

Supplementary Movies S6 (.mp4 format). Intelligent parallel manipulation of droplets of different volumes (microscope, 1X)

Supplementary Movies S7 (.mp4 format). Intelligent parallel manipulation of droplets of different volumes (software, 3X)

Supplementary Movies S8 (.mp4 format). Intelligent parallel control of algal and medium droplets (microscope, 3X)

Supplementary Movies S9 (.mp4 format). Intelligent parallel control of algal and medium droplets (software, 3X)

S1 Optoelectrowetting digital microfluidic platform

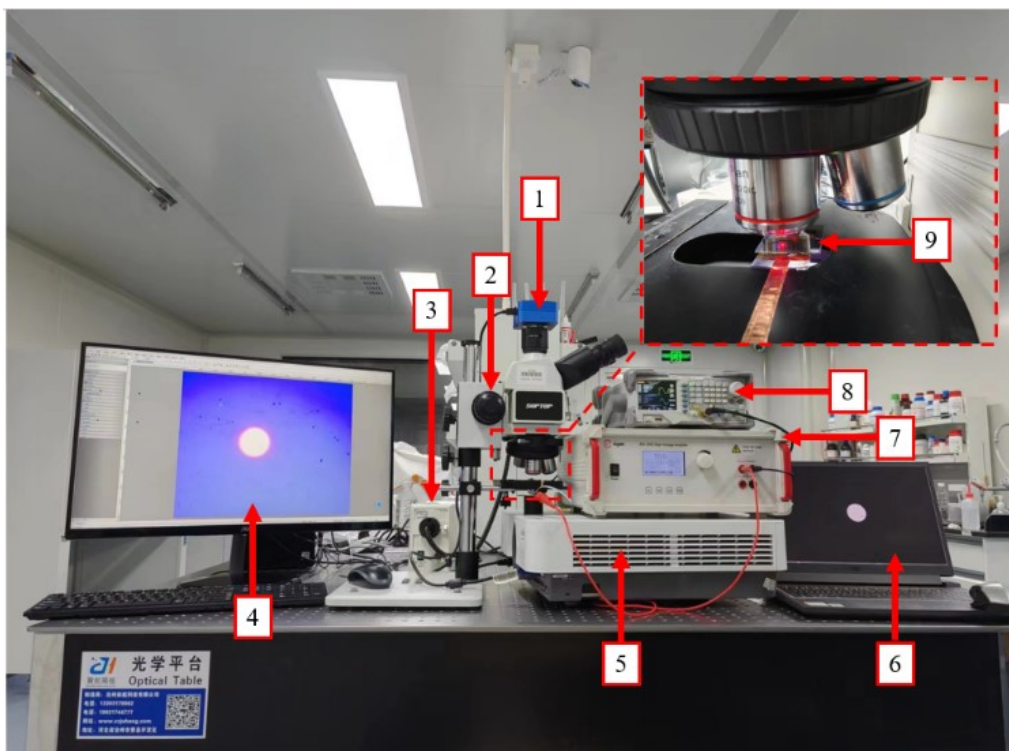


Fig. S1. Optoelectrowetting digital microfluidic platform. Components are as follows: (1) CCD camera; (2) upright microscope; (3) camera light source; (4) computer 1; (5) projector; (6) computer 2; (7) signal amplifier; (8) function signal generator; (9) OEW chip.

S2 OICS software interface

The OICS program areas 1-2 serve as the primary adjustment and control interfaces, enabling user-system interaction. This section includes essential functionalities such as weight import, detection options, parameter adjustment, optical pattern selection, trajectory tracking, and movement speed control. Through the control panel, users can manually adjust parameters like droplet trajectory and speed, providing intuitive control over system behavior. Emphasis is placed on user-friendly design to ensure that experimental setup and operation are both accessible and straightforward. The optical pattern selection feature allows for choosing various optical shapes, including rectangular, circular, and ring patterns. Each shape affects the electrowetting force surrounding the droplet, facilitating different levels of droplet manipulation. The trajectory tracking feature offers individualized control over single droplets, enabling interactive manipulation of targeted droplets to move according to the researcher's intentions, thus achieving customized droplet control. Additionally, movement speed adjustments allow for precise control of droplet velocity along the set trajectory. In area 3, the detection visualization window provides real-time monitoring and displays the output detection images. Researchers can observe the droplet

numbers, positions, behaviors, and changes in optical patterns, offering direct feedback. Area 4 outputs this information. Finally, area 5, the optical pattern generation area, transforms the algorithm's detection results into optical patterns displayed on a black canvas. The projection system then casts these optical patterns onto the chip surface.

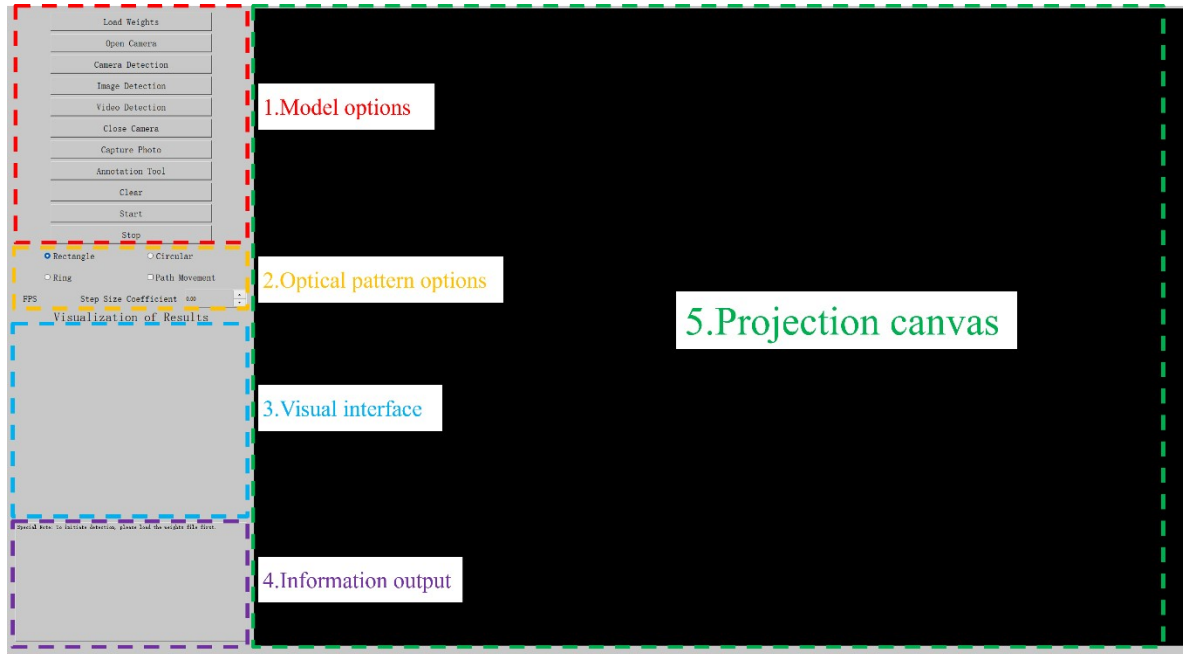


Fig. S2. Software interface. The software interface is divided into five main areas. Areas 1 and 2 serve as the user interaction interface, encompassing features such as weight import, detection options, parameter adjustments, optical spot selection, trajectory tracking, and movement speed controls. Areas 3 and 4 function as output sections: area 3 displays real-time images within the microfluidic chip, including detection result information, while area 4 outputs this information to assist operators in monitoring the experimental process. Area 5 serves as the projection interface, where droplet detection results are presented as optical patterns, designed for projecting virtual electrodes.

S3 Overview of OICS operation process

We present an overview of the primary operating workflow of the system, which includes the detection and tracking algorithms, trajectory generation, trajectory control, as well as self-feedback and error correction mechanisms.

OICS main algorithm.

- Input: Video file path or camera video stream, detection model, device configuration parameters
 - Output: Saved video with detection results, droplet and spot data file
1. Initialize UI and basic settings

2. Load model and tracker
3. Process each frame
4. Track generation
5. Spot Control and Rendering
6. End Video Detection and Release Resources

Detection and Tracking Algorithm

- Input: Current video frame, detection mode, device parameter, detection configuration, tracker.
- Return: Video frame with detection and tracking results, droplet tracking data ('cur_droplet')

Loop: While video capture 'cap' is not finished

1. Read the video frame 'img';
 - 1.1 if reading fails:
 - 1.1.1 exit the loop.
2. Update frame count and per-frame processing time for calculating relevant speed.
3. Save spot data file every few frames.

Instruction Sequence:

4. detect droplets ← detect_droplets (img, model, device, opt)

- Input: 'img' current frame, 'model' detection model, 'device' device, 'opt' detection configuration
- Return: Detection results 'pred' for subsequent tracking

5. track droplets ← track_droplets (img, pred)

- Input: current frame and detection results
- Return: Tracking results ('cur_droplet') including center coordinates, aspect ratio, detection ID, speed, and path info

6. Save the processed detection frame to the video file
7. Display detection results, resize the frame and show in the UI

Path Planning Algorithm

- Input: droplet data, endpoint data
 - Output: Track
1. Initialize endpoint information for each droplet
 2. if draw track:

2.1 return track data (with IDs)

3. else:

3.1 path planning

- Input: Droplet data, endpoint data
- Return: tracks (with IDs)

4. For each droplet in droplet

- 4.1 Update the existing track data and relevant dictionary, assign each droplet its path

4.2 Store each droplet path in the global variable ('droplet_tracks') for future tracking

Spot Control Algorithm

- Input: Droplet paths ('droplet_tracks'), scaling factor ('scale_rate'), current droplet tracking data ('cur_droplet')
- Return: Updated spot position and shape

The main components of spot generation and control:

1. For each droplet (with id) in 'cur_droplet':
 - 1.1 if the id exists in 'droplet_tracks':
 - 1.1.1 obtain current track info for each droplet
 - 1.1.2 Calculate current droplet coordinates
 - 1.1.3 Calculate the distance ('d2s': droplet to spot) and compare with threshold
 - 1.1.4 If the distance 'd2s' exceeds threshold:
 - a. Reset spot position to match droplet location
 - b. Record the mismatch count of this droplet
 - 1.1.5 Calculate the distance ('d2t': droplet to nearest point of track)
 - 1.1.6 Calculate step size 'step_x' and 'step_y' according to 'd2t' and the info of droplet
 - 1.1.7 if 'd2t' < threshold:
 - a. coordinate of spot ← the coordinate of nearest point of track
 - b. update the nearest track point
 - c. if the length of track is none:
 - i. remove the current track
 - ii. show completion info in UI
 - 1.1.8 Save tracking data for both droplet and spot
 - 1.1.9 Update the spot position based on step size and scaling factor
 - 1.1.10 Display updated canvas on UI
 - 1.1.11 Update track time and remove completed track
 - 1.2 else if 'droplet_tracks' is None:
 - 1.2.1 Clear tracking data, uncheck path planning option
 - 1.2.2 Draw static spot at current droplet positions

S4 Impact of luminance on detection

Luminance values play a crucial role in the application of deep learning for droplet detection. As shown in the figure, varying luminance intensities significantly impact droplet visibility and edge clarity within images. At lower luminance levels (e.g., 0.1% and 1%), droplet edges appear sharper, and image contrast is notably enhanced, facilitating model recognition and detection of droplets. However, as luminance increases (e.g., 2% and 5%), droplet contours become more blurred or even overexposed, which hinders the deep learning model's ability to accurately identify boundaries and features, thereby increasing detection error. Selecting an appropriate luminance level helps reduce background noise and enhances the visibility of droplet features, thus improving detection accuracy and robustness.

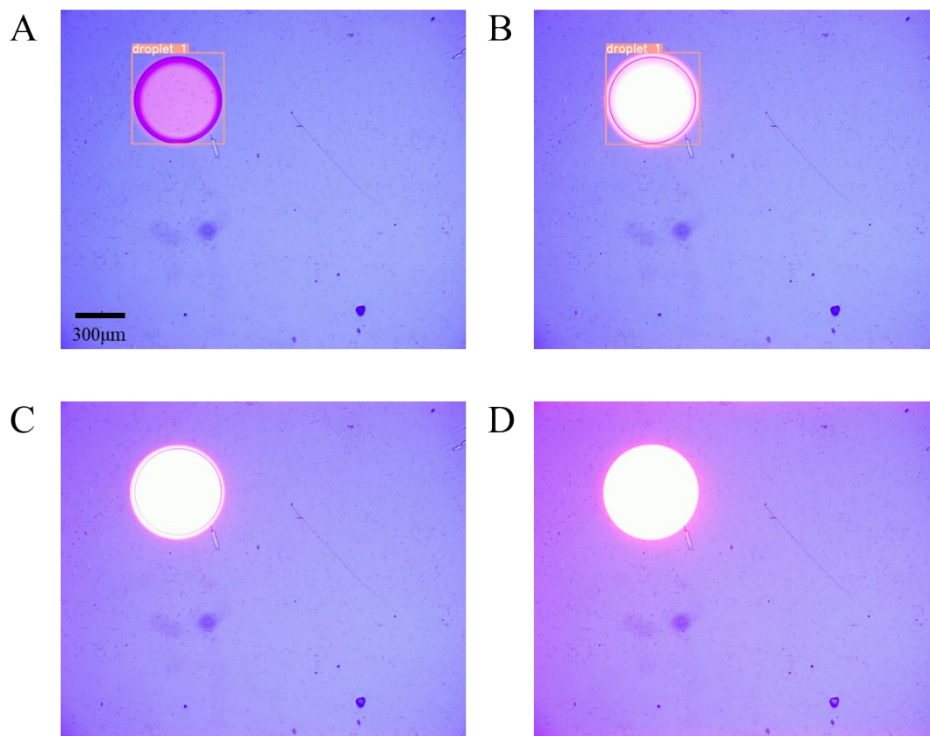


Fig. S3. Effect of different luminance levels on detection. (A) 0.1% optical density filter; (B) 1% optical density filter; (C) 2% optical density filter; (D) 5% optical density filter.

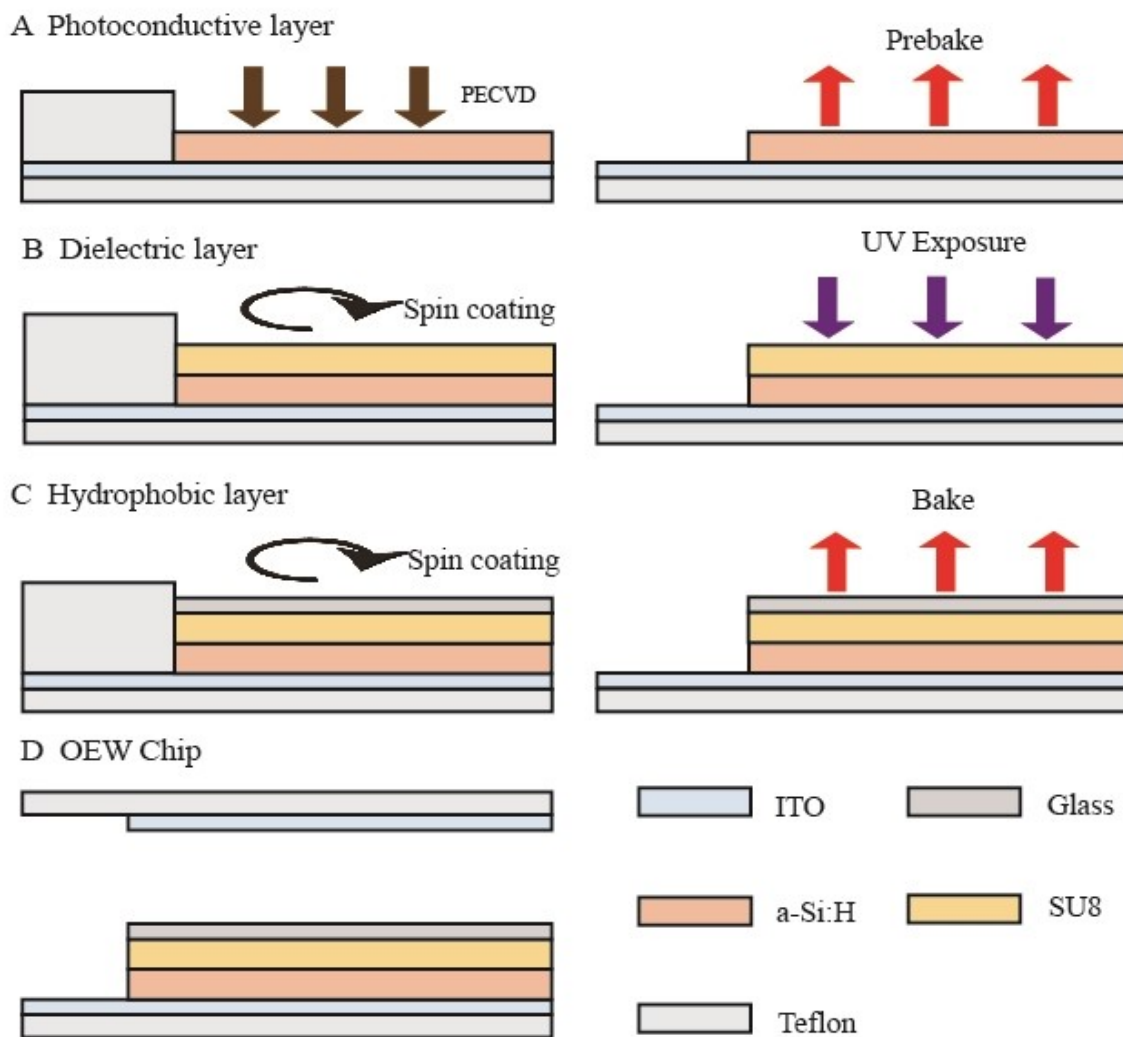
S5 Chip fabrication process

Photoconductive layer: Prior to deposition, conductive glass was sequentially ultrasonically cleaned using acetone solution, alcohol, and deionized water. Each cleaning step lasted 5 minutes to ensure thorough removal of surface impurities and contaminants. After cleaning, high-pressure nitrogen gas was used to blow away any remaining water droplets on the glass surface, followed by drying in an oven to achieve complete dryness of the glass substrate. To reserve an area for connection with the signal generator using conductive tape, a rectangular mask was applied to cover part of the ITO conductive glass, designating a conductive region for subsequent experiments. Next, a 1 μm layer of intrinsic a-Si was deposited on the ITO side of the glass to serve as the photo-generated carrier response layer.

Dielectric Layer: A pipette was used to apply 200 μL of SU-8 2002 photoresist onto the prepared light-guiding layer on the ITO glass, allowing the photoresist to spread evenly across the entire chip. The chip was then placed on a spin coater and spun at 3500 rpm for 30 seconds. The coated sample was baked on a hot plate at 95°C for 120 seconds, and after exposure, a 1 μm -thick SU-8 photoresist layer was achieved.

Hydrophobic Layer: To impart hydrophobicity to the chip and increase the initial contact angle, Fluorinert FC-40 (3M) was selected as a solvent, and a 5:1 solvent-to-solute ratio was used to dilute Teflon AF1600 solution.

The lower substrate was secured on the spin coater chuck, and a 1% Teflon AF solution was applied using a dropper, starting at the center of the substrate and covering the entire surface. The spin coater was then operated at 4000 rpm for 30 seconds. The substrate was baked in an oven at 110°C for 15 minutes and at 165°C for an additional 15 minutes, resulting in a hydrophobic Teflon layer approximately 50 nm thick.



+

Fig. S4. Chip fabrication process. (A) Preparation of the light-guiding layer; (B) Preparation of the dielectric layer; (C) Preparation of the hydrophobic layer; (D) Complete OEW structure.

S6 OEW chip

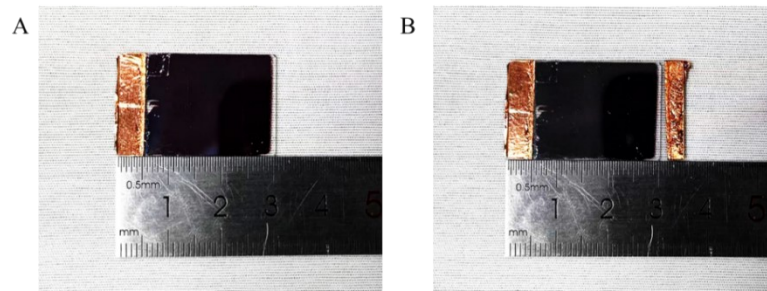


Fig. S5. Images of the OEW chip. (A) Single-sided view; (B) Encapsulated view.

S7 Photolithography process for droplet storage reservoir

Substrate pretreatment: Place the silicon wafer in a boiling mixed acid solution for 2 hours. After cooling, rinse the wafer and transfer it to a glass petri dish. Clean the silicon wafer repeatedly in an ultrasonic cleaner using acetone solution to remove organic residues from the surface. Next, immerse the silicon wafer in an anhydrous ethanol solution to clean inorganic residues, followed by rinsing with deionized water and drying with nitrogen gas.

Photoresist application: Pour photoresist onto the pretreated ITO glass to spread it evenly. Spin coat the ITO glass at 500 rpm for 6 seconds, followed by 1820 rpm for 20 seconds to achieve a 50 μm -thick layer.

Pre-bake: Remove the spin-coated silicon wafer with photoresist and place it horizontally in a fume hood for 3–5 minutes. Perform a soft bake by heating at 65°C for 3 minutes and at 100°C for 8 minutes. Cool to room temperature and gently grip the edges with plastic tweezers to confirm that the photoresist has solidified.

Exposure: After cooling, cover the ITO glass with a photomask containing a U-groove array structure for the observation area. Place a transparent acrylic plate on top to ensure close contact between the photomask and the ITO glass, and expose the assembly under a photolithography machine for 6 seconds.

Soft bake: Place the exposed ITO glass on a hot plate at 65°C for 3 minutes, followed by heating at 95°C for 8 minutes to complete the soft bake.

Development: Place the silicon wafer in a glass petri dish, add developer solution, and agitate for 5 minutes to develop the photoresist pattern. If the photoresist is thick, replace the developer solution to avoid saturation. Rinse the developed silicon wafer with acetone solution and inspect the clarity of the developed pattern under a microscope. After development, rinse the wafer with ample deionized water and dry with nitrogen gas.

Post-bake: Place the developed silicon wafer on a hot plate and heat at 100°C for 30 minutes. Once cooled, wrap the chip in aluminum foil for storage.

Hydrophobic layer spin-coating: Use a pipette to apply 200 μL of 1% Teflon spin-coating solution onto the

prepared substrate. Spin coat at 4000 rpm for 30 seconds to obtain a Teflon hydrophobic layer approximately 50 nm thick.

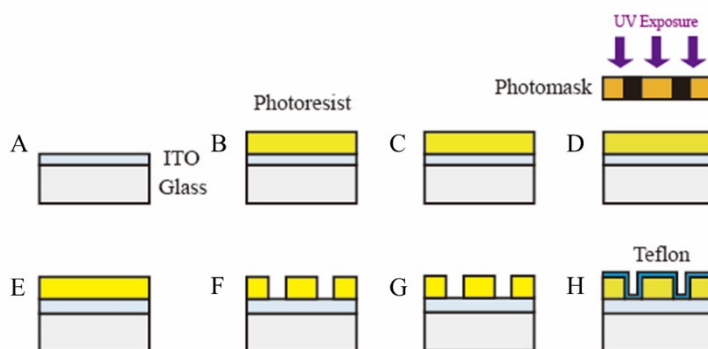


Fig. S6. Photolithography Process for Droplet Storage Reservoir. (A) Substrate pretreatment; (B) Photoresist application; (C) Pre-bake; (D) Exposure; (E) Soft bake; (F) Development; (G) Post-bake; (H) Hydrophobic layer spin-coating.

S8 Model comparison and training

In this study, our detection targets are micro-scale droplets of various colors and algal droplets. Algal droplets are distinguished by containing minuscule algal cells within each droplet, which introduces the challenge of detecting fine details within droplets across diverse backgrounds, making detection and classification more demanding for the model. To address this, we compared seven mainstream object detection models: SSD (Single Shot MultiBox Detector), Faster-RCNN (Faster Region-based Convolutional Neural Network), RT-DERT (Real-Time Detection Transformer), and several series within the YOLO (You Only Look Once) framework, including YOLOv4 (YOLOv4 and YOLOv4-tiny), YOLOv5 (YOLOv5-n, YOLOv5-s, YOLOv5-m), YOLOx (YOLOx-nano, YOLOx-tiny, YOLOx-s), and YOLOv8 (YOLOv8-n, YOLOv8-s, YOLOv8-m, YOLOv8-n-swintransformer).

As shown in Fig. S7A, the basic workflow for droplet detection involves inputting droplet images into a convolutional neural network (CNN). Through a series of upsampling, feature extraction modules (such as the Cross Stage Partial Block (C3) and the Spatial Pyramid Pooling – Fast (SPPF)), the detection module produces output results that include the class, confidence, and location (x, y, w, h) of each droplet. This architecture, with its effective feature extraction and fusion, ensures model robustness when processing droplet images of varying shapes and backgrounds. A comparison with other mainstream detection models (such as SSD, Faster-RCNN, and RT-DETR) on inference time and mean average precision (mAP) shows that the YOLOv5 series achieves a favorable balance between inference time and accuracy, with times ranging from 2-10 ms, as shown in Fig. S7B. This demonstrates

that the YOLOv5 model, with its real-time detection capability and high accuracy, is well-suited for droplet detection tasks.

The initial learning rate for our trained droplet detection model was set to 0.001, and a cosine annealing strategy was applied to gradually reduce the learning rate, aiding model convergence. The batch size was set to 32 to balance memory usage and training speed. The model was trained for 300 epochs, and the optimal model weights were selected based on validation set performance. During training, the Adam optimizer was used, with a momentum of 0.937 and a weight decay of 0.0005. To address class imbalance, we employed a weighted cross-entropy loss function to monitor the model's loss performance, as illustrated in Fig. S7C. If validation loss did not decrease over five consecutive epochs, the learning rate was adjusted to 0.1 times the original. At the end of each epoch, model performance was evaluated on the validation set using mean average precision (mAP), and the model with the best performance was saved, as shown in Fig. S7D. Ultimately, the YOLO model achieved 98.5% mAP on the validation set, enabling accurate and real-time detection of droplet positions and sizes, as depicted in Fig. S7E.

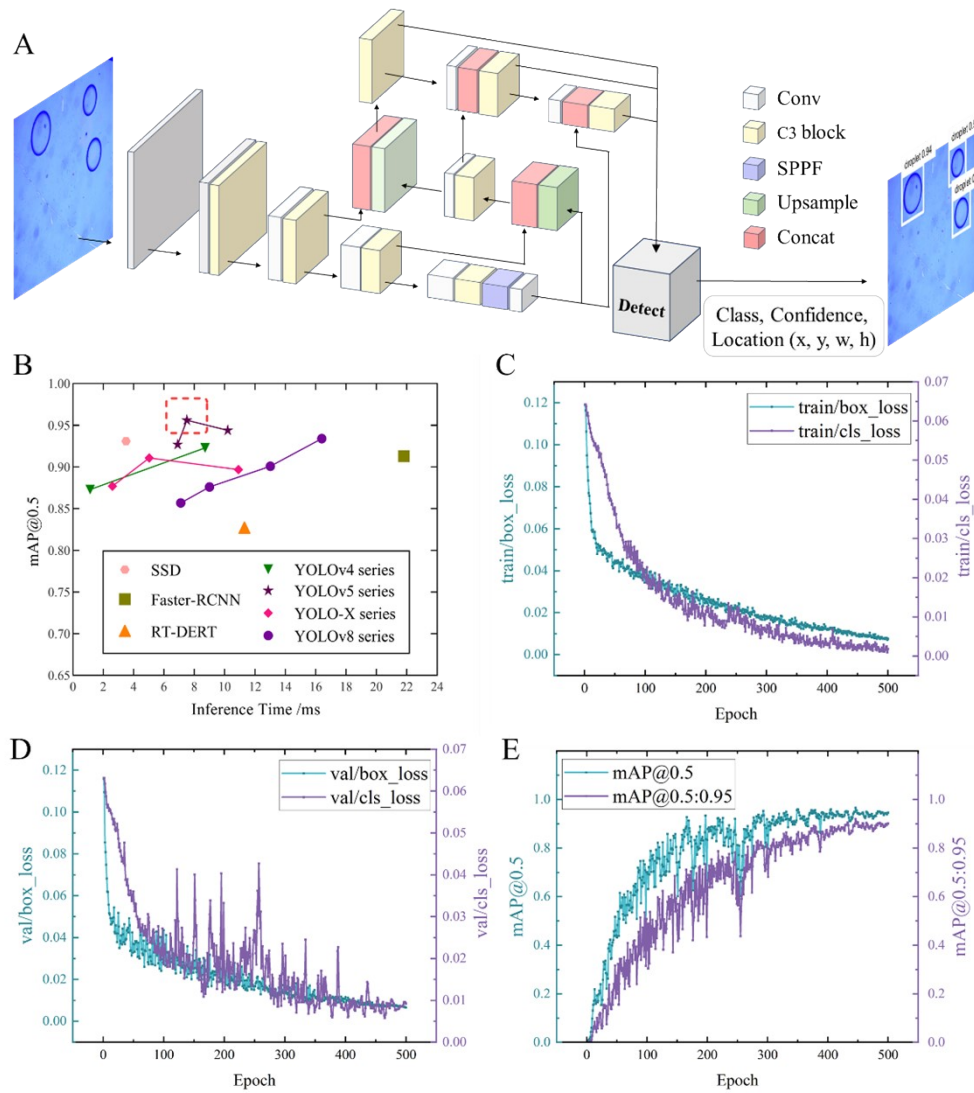


Fig. S7 Model comparison analysis. A: YOLO model architecture. Droplet images are fed into the convolutional neural network, where a series of upsampling and downsampling operations are applied to extract features, allowing for the identification of droplet categories and location information. B: Comparison of mainstream object detection models, selecting the model that performs best on an independent test set, which is then applied to subsequent experiments. C: The loss value changes during the training process of the YOLOv5s model. D: The mean average precision on the validation set during the training of the YOLOv5s model. E: The validation accuracy at different confidence thresholds during the training of the YOLOv5s model.

S9 Tracking and matching process of the ByteTrack algorithm

The ByteTrack algorithm used for object tracking achieves accurate trajectory prediction and matching through Kalman filtering and an IoU (Intersection over Union) based matching strategy. In the tracking process, the detection boxes and ID information from the previous frame are first obtained and input into the Hungarian algorithm, which

predicts their possible positions in the current frame and stores these as hypotheses. The current frame image is then processed by the YOLOv5 model, which outputs the predicted bounding boxes (D) for the targets. These predictions are divided into two sets: high-confidence boxes (light green in the figure) and low-confidence boxes (orange in the figure) in a process known as confidence sorting. Matching between predictions and IDs occurs in two steps. In the first matching step, high-confidence prediction boxes are compared with the hypotheses using IoU; if the IoU exceeds a set threshold, the corresponding ID of the hypothesis is assigned to the matched prediction box. In the second matching step, low-confidence detection boxes are sequentially matched with the remaining unmatched hypotheses, and IDs are assigned to the low-confidence boxes. If a prediction box in D has no corresponding ID, it is assigned a new ID (light blue in the figure). If a hypothesis has no matching prediction box, it is assumed that the target has either left the field of view or is occluded. If this unmatched hypothesis remains unmatched for five consecutive frames, its ID's trajectory is terminated.

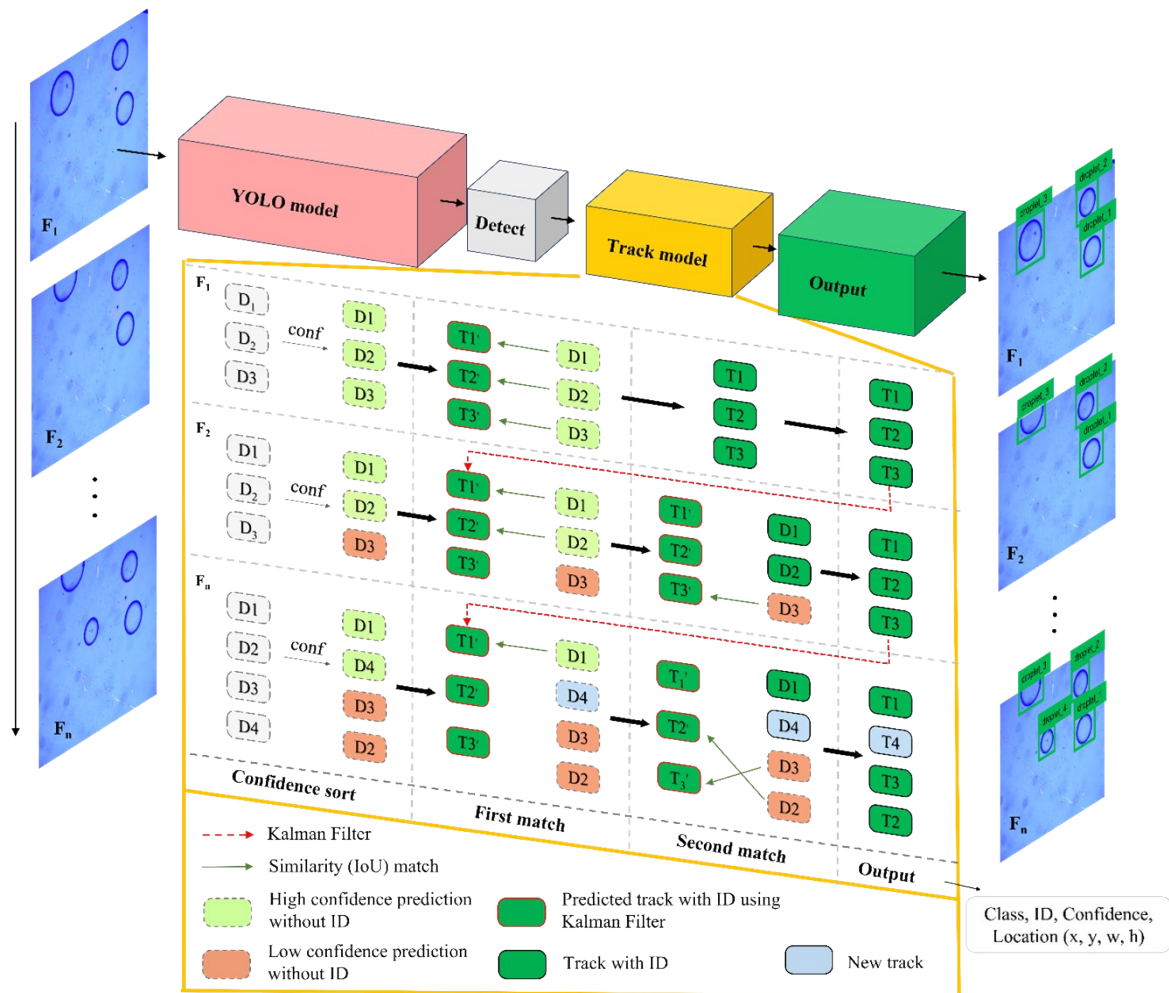


Fig. S8. Overview of the OICS detection and tracking architecture.

S10 Comparison of droplet speed at different frequencies

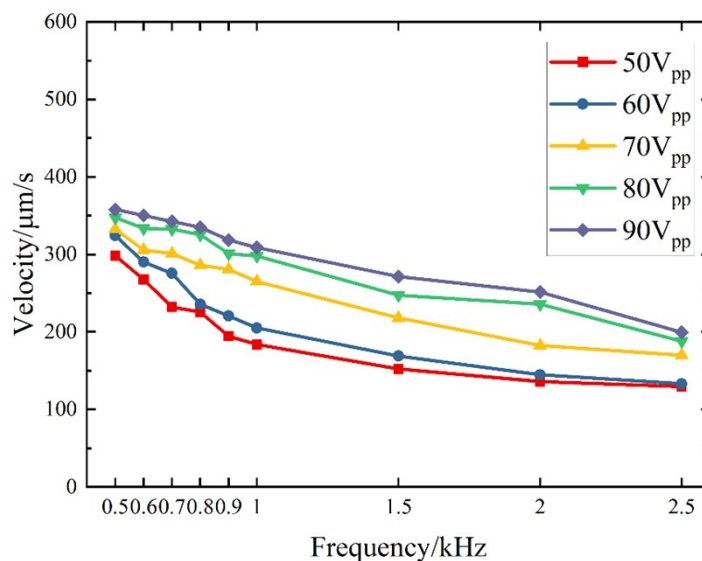


Fig. S9. Comparison of droplet speed at different frequencies We investigated the effect of various frequencies—500 Hz, 600 Hz, 700 Hz, 800 Hz, 900 Hz, 1 kHz, 1.5 kHz, 2 kHz, and 2.5 kHz—on droplet speed. The results indicate a downward trend in droplet speed as frequency increases. For example, at 50 V_{pp}, droplet speed at high frequencies is reduced by half compared to lower frequencies. This demonstrates that higher frequencies significantly decrease droplet speed. Conversely, as voltage increases, the electric field strength also increases, resulting in faster droplet movement. This suggests that higher voltages provide a stronger electric field force, thereby promoting more rapid droplet motion.

S11 Droplet behavior at different voltages

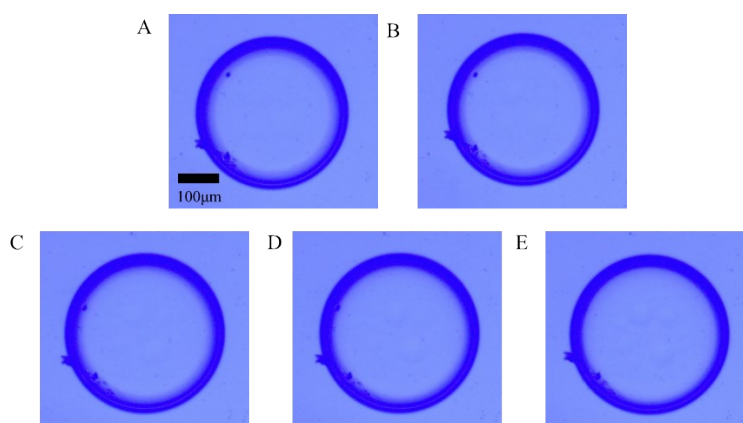


Fig. S10. Droplet at different voltages. (A) 50V_{pp}; (B) 60V_{pp}; (C) 70V_{pp}; (D) 80V_{pp}; (E) 90V_{pp}. As the applied voltage increases, the electric field strength also increases, making dielectric breakdown of the droplet more likely. When the voltage is within the range of 50-70V_{pp}, the droplet maintains a normal shape. However, at

voltages above $80V_{pp}$, small bubbles appear within the droplet, indicating the onset of hydrolysis. For biological applications, a lower operating voltage is preferred to maintain droplet stability.

S12 Culturing with 0X0 and 1X1 medium containing dye in 96-well plates

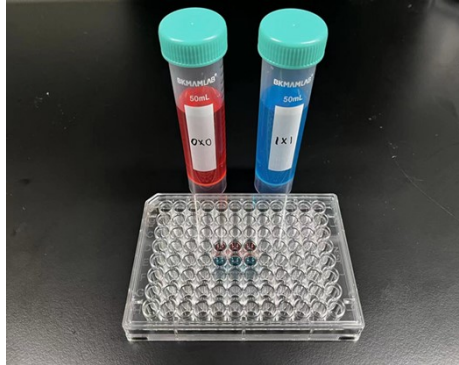


Fig. S11. Preparation of dyed 0X0 and 1X1 media and 96-well plate culturing. To prepare the culture medium solution, first weigh 1633 mg of BG11 medium powder and dissolve it in 1000 mL of deionized water to make two bottles of BG11 medium solution. Then, according to the two experimental conditions, weigh the specified amounts of sodium nitrate and potassium phosphate tribasic trihydrate, dissolving them into the prepared medium solution. Adjust the pH to 7.1 with diluted hydrochloric acid, then sterilize the solution in an autoclave at 121°C for 15 minutes. After sterilization, allow the medium solution to cool to room temperature. Use part of the solution for cell culturing, adding dye as needed, and store the remaining solution in a refrigerator for low-temperature preservation.

S13 Characterization of *C. vulgaris* cultured in 96-well plates on hemocytometer

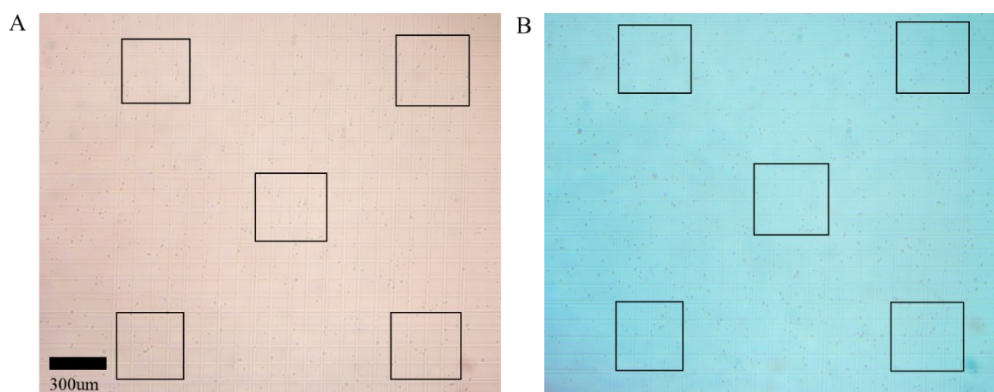


Fig. S12. Characterization of *C. vulgaris* cultured in 96-well plates on hemocytometer. (A) 0NX0P medium hemocytometer; (B) 1NX1P medium hemocytometer. The areas outlined by black boxes in the images represent the counting regions.

S14 Comparison of projected optical patterns

To investigate the impact of optical pattern shapes on droplet manipulation, we designed three experimental groups using different optical patterns (ring and circular) to control droplets. Based on the experimental conclusions in Fig. 3, each droplet, approximately 530 μm in diameter, was alternately manipulated using these two optical patterns in a back-and-forth process (see Fig. S14A and S14B). This allowed for further analysis of the influence of ring-shaped patterns on droplet manipulation accuracy. As shown in Fig. S14C, there is a slight difference in performance between ring and circular optical patterns. The relative standard deviation (RSD) of each experiment group indicates that the droplet movement accuracy for both patterns is similar, with fluctuations within a 5% range across the three groups. Additionally, Fig. S14D illustrates the coordinate deviation of droplets during movement, showing a deviation range of 88 μm for the ring pattern and 74 μm for the circular pattern, both of which are less than 2% of the droplet diameter. Although some differences exist, both patterns provide acceptable control over droplet manipulation and are suitable for practical applications where precision requirements are met.

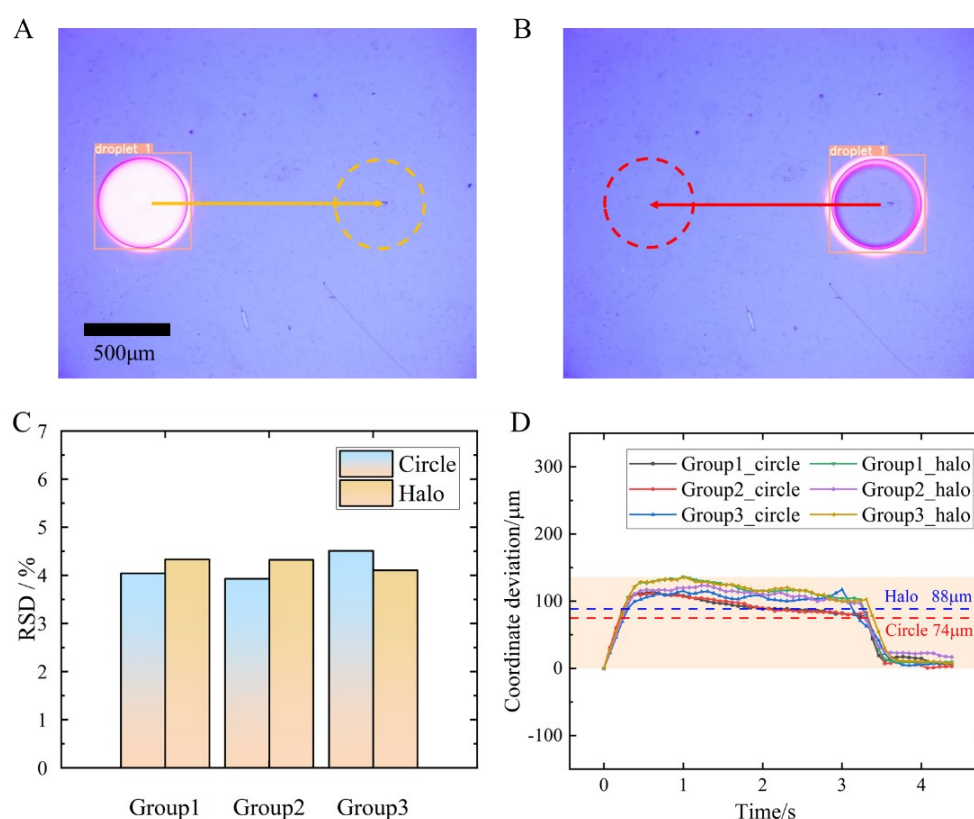


Fig. S13 Comparison of projected optical patterns. (A-B) Two different optical patterns were used alternately to control the droplet; (C) RSD (Relative Standard Deviation) for ring and circular-driven droplets. The RSD values for the circular pattern range from 3.93% to 4.51%, while the RSD values for the ring pattern are slightly

higher, ranging from 4.10% to 4.33%; (D) Control effect of ring and circular optical patterns on droplet manipulation. The average deviation for the ring pattern is approximately 88 μm , while the circular pattern has an average deviation of about 74 μm , as indicated by the dashed lines in the figure.

Supplementary Table S1 Customized BG11 medium composition table

Component	Concentration(mg/L)	Component	Concentration(mg/L)
MgSO₄	36.6	MnCl ₂ ·H ₂ O	1.81
CaCl ₂ ·2H ₂ O	27.2	ZnSO ₄ ·7H ₂ O	0.22
Na ₂ CO ₃	20	CuSO ₄ ·5H ₂ O	0.08
Citric acid	6	Na ₂ MoO ₄ ·2H ₂ O	0.39
EDTA	1	CoCl ₂ ·6H ₂ O	0.0409
Ferric ammonium citrate	6	H ₃ BO ₃	2.86